



# On the fast kinetics of B2–L2<sub>1</sub> ordering in Ni–Co–Mn–In metamagnetic shape memory alloys



Yuhao Wang<sup>a,\*</sup>, Daniel Salas<sup>a</sup>, Thien C. Duong<sup>a</sup>, Bharat Medasani<sup>b</sup>, Anjana Talapatra<sup>a</sup>, Yang Ren<sup>c</sup>, Yuriy I. Chumlyakov<sup>d</sup>, Ibrahim Karaman<sup>a</sup>, Raymundo Arróyave<sup>a</sup>

<sup>a</sup> Department of Materials Science and Engineering, Texas A&M University, College Station, TX 77843-3123, United States

<sup>b</sup> Pacific Northwest National Laboratory, 902 Battelle Blvd, Richland, WA 99354, United States

<sup>c</sup> X-ray Science Division, Advanced Photon Source, Argonne National Laboratory, Lemont, IL 60439, United States

<sup>d</sup> Siberian Physical and Technical Institute, Tomsk State University, 634050, Tomsk, Russia

## ARTICLE INFO

### Article history:

Received 17 September 2018

Received in revised form

26 November 2018

Accepted 3 December 2018

Available online 8 December 2018

### Keywords:

First-principles calculations

Meta-magnetic shape memory alloys

Vacancy evolution

Order/disorder kinetics

Martensitic transformation

## ABSTRACT

B2–L2<sub>1</sub> configurational order resulting from thermal processing of Ni–Co–Mn–In Heusler alloys is one of the main factors defining the characteristics of the martensitic transformation experienced by these alloys. While the effects of the quenched-in disorder on the martensitic transformation have been extensively investigated, the kinetics of the ordering process is not well known and mostly inferred from the indirect results such as the dependence of the martensitic transformation or magnetic transition temperatures to thermal processing. However, recent results suggested that the kinetics of B2–L2<sub>1</sub> ordering could have a more significant role than expected in the final state of the material and its functional properties. In the current work, an attempt has been made to investigate the kinetics of B2–L2<sub>1</sub> ordering in order to evaluate the dependence of the quenched-in disorder on the different variables of the thermal procedures. Results showed that ordering rate has a strong dependence on annealing temperature. Below 600 K, slow kinetics is forcing the crystal to always contain a certain amount of quenched-in disorder at room temperature. Between 600 K and 750 K, kinetics is fast enough to reach thermal equilibrium state within tens of minutes during the annealing process. Above 750 K, kinetics is very fast and thermal equilibrium can be reached during heating, so no isothermal holding is required. These predictions have been confirmed using differential scanning calorimetry and in-situ high-energy X-Ray diffraction measurements for non-direct estimations of the degree of order.

© 2018 Elsevier B.V. All rights reserved.

## 1. Introduction

### 1.1. Overview

Nickel–Manganese based Meta-Magnetic Shape Memory Alloys (MMSMAs) are a special kind of magnetic shape memory alloys with the distinctive characteristic that the parent (austenite), and product (martensite) phases exhibit very different magnetic ordering—e.g. Ferromagnetic (FM)/Antiferromagnetic (AFM). Upon martensitic transformation (MT), MMSMAs thus undergo significant changes in their magnetization state. The resulting magneto-structural transformation (MST) leads to phenomena such as (magnetic) shape memory effect [1], superelasticity, or ferrocaloric

effects [2]. Because of the strong magneto-structural coupling, the onset of the MT can be manipulated through the application of an external magnetic field [3–5], leading to complex phenomena—e.g. giant magnetocaloric effect (MCE) [6–9] and large magnetoresistance [10,11]—which can in turn potentially enable a wide range of applications [12].

In this work, we focus on Mn-rich Co-doped Ni–Co–Mn–In Heusler MMSMAs. In this system, the (Heusler) stoichiometric composition Ni<sub>2</sub>MnIn does not transform [13], while the (AFM) NiMn binary subsystem undergoes a MT at elevated temperatures [14] (~1000 K), without a change in the magnetic state accompanying the martensitic transformation. Mn-rich Ni<sub>50</sub>Mn<sub>50–x</sub>In<sub>x</sub> do undergo MT [15], which occurs at lower temperatures than the MT

\* Corresponding author.

E-mail address: [yuhao\\_wang@tamu.edu](mailto:yuhao_wang@tamu.edu) (Y. Wang).

of NiMn binary as replacement of Mn by In decreases the electron-to-atom ratio [14]. Substituting a small amount of Ni by Co enhances  $T_C$  of the austenite phase, stabilizing it against martensite, reducing, in turn, MT but increasing the change in magnetization through the MT [16,17].

$\text{Ni}_{45}\text{Co}_5\text{Mn}_{50-x}\text{In}_x$  alloys with  $x$  around 13.3 exhibit a MT at room temperature, accompanied by a transition from a cubic FM state (austenite has a  $T_C \sim 380$  K) to a body-centered tetragonal (modulated or non-modulated) weakly magnetic martensitic state [15,18]. The different magnetic ordering behaviors of austenite and martensite have their origin on the intensity of the Ruderman-Kittel-Kasuya-Yosida (RKKY)-exchange interactions between Mn atoms and its variation [19] due to changes in Mn–Mn interatomic distances brought about by changes in the structural parameters as a result of the MT. In the case of the Ni–Co–Mn–In alloy under study, the austenite is FM, while competition between FM and AFM interactions in martensite often results in superparamagnetic [20] behavior at room temperature.

The strength of the FM/AFM magnetic exchange interactions in Ni–Co–Mn–In Heusler alloys can be further modified by the (local) configurational order in the lattice due to the tight linkage between the magnetic and structural transformations. Monroe, Karaman et al. [21] showed that the onset of the MST can be dramatically altered by changes in the microstructure occurring during thermal processing. While it is generally understood that the associated microstructural processes are related to modifications in the local configurational order in the system, the identity of the microstructural features affecting the thermostability of the MST remains unclear.

### 1.2. Order-disorder transition in Ni–Co–Mn–In alloys

Heusler alloys,  $\text{X}_2\text{YZ}$ , are formed by three atomic species with a 2:1:1 stoichiometry (and three crystallographic sublattices) and can present different phases depending on the distribution of these atomic species through the crystal [22]. As temperature increases, from the low-temperature grown state, Heusler alloys may undergo a series of order-disorder transitions (ODO) from  $\text{L}_{21}$ , through B2, to A2/BCC depending on the degree of symmetry in site occupancies between the X, Y and Z sublattices.

Previous works on the ODO transitions of the Ni–Mn-based MMSMAs have investigated the temperature-dependence of the order parameter computationally [23] and experimentally [24]. Such works have shown that, in the present  $\text{Ni}_{45}\text{Co}_5\text{Mn}_{50-x}\text{In}_x$  alloy the B2– $\text{L}_{21}$  ODO temperature (the system melts before completely disordering to A2),  $T_{\text{B2-L}_{21}}$ , lays around 896 K [25] and  $\text{L}_{21}$  overall degree of order,  $S_{\text{L}_{21}}$ , increases on cooling as  $S_{\text{L}_{21}} \propto (1 - T/T_{\text{B2-L}_{21}})^\beta$  [24,26], where  $\beta$  is a critical exponent.  $T_{\text{B2-L}_{21}}$  is low enough to permit the quenching of the high-temperature B2 ordering state by fast cooling the material to room temperature, which means that the final configurational order present at room temperature can be tuned [21,27].

Many properties of the Ni–Co–Mn–In alloys and their MST transformations depend on the quenched-in disorder through the different characteristics of the B2 and  $\text{L}_{21}$  phases. To begin with, increasing degree of order changes the distribution of Mn atoms through the crystal. Since Mn–Mn magnetic exchange in this systems follows RKKY-type behavior, with oscillations between FM and AFM-type coupling, ODO has significant effects on the overall distribution of FM/AFM interactions in the lattice, and this, in turn, changes the stability of the austenite relative to the martensite phase. This dependence of the MST temperatures on the degree of order through tuning of magnetic ordering is a phenomenon shared with other ferromagnetic shape memory alloys [28,29] and

has been exploited recently to optimize, for example, the magnetic cooling characteristics in Ni–Mn-based Heusler systems [30].

### 1.3. Dependence of martensitic transformation temperatures on thermal treatments in Ni–Co–Mn–In alloys

Recently, different methods of engineering the characteristics of the magneto-structural transformation in Ni–Co–Mn–In alloys have been broadly investigated. The strong dependence of MST characteristics on composition changes and the different thermal processing parameters such as cooling rate, temperature and duration of the heat treatment, was revealed through the work of several groups. Ito et al. [25] compared the MST properties of the samples annealed at two different temperatures followed by rapid quenching to obtain two different ordered states and concluded that the more ordered samples exhibited higher  $T_C$ ; lower  $M_S$  and different magnetic moment and crystalline structure of the martensite. Kustov et al. [31] reported a strong correlation between the total entropy upon MST change and  $T_C - M_S$  ( $M_S$ : Martensite start temperature).

Later, Monroe et al. [21] carried out an extensive investigation of the effect of annealing temperature on the characteristics of the MST. As in previous works [25,31], they observed that  $M_S$  decreased and  $T_C$  increased on decreasing Secondary Heat Treatment (SecHT) temperatures. In addition, Monroe et al. described the appearance of the strain-glass for the austenite phase and the low-temperature spin-glass for the martensite phase and found a correlation between the degree of order/SecHT temperature, the suppression of the MT, and the glassy features associated with the strain-glass and spin-glass transitions. In their work, Monroe et al. assumed that the dramatic changes in the transformation behavior in the alloy was exclusively due to the (equilibrium) degree of order achieved at different SecHT temperatures with fixed annealing times of 3 h—deemed sufficient to achieve the equilibrium order state at each temperature [24]. That is, they concluded that the phase diagram depicting the onset of the different transitions (martensitic, magnetic, etc.) corresponded to equilibrium.

A recent investigation conducted by Bruno et al. [32], however, showed that much longer annealing times than the ones used by Monroe et al. [21] resulted in non-trivial changes in  $M_S$ . Notably, they observed non-monotonic changes in  $M_S$  with time when annealing at 773 K, with  $M_S$  decreasing upon annealing for 0.25 h, followed by an increase at longer annealing times. To explain this non-monotonic behavior, Bruno et al. suggested that the initial decrease in  $M_S$  was a consequence of the ODO transition, whereas the subsequent increase could have been due to vacancy annihilation once ordering had finished. This explanation was in good agreement with previous observations on the effect of order [4,33,34] and vacancy concentration [35,36] on MT properties. However, since  $M_S$  was observed to decrease (and then increase) long after the first 3 hours for annealing treatments performed at 573 and 673 K, for the change in the degree of order to be responsible of the observed changes in  $M_S$ , it was necessary to invoke slow ODO kinetics. Regardless of the operating kinetic processes and their rate, these results suggest that the earlier observations by Monroe et al. cannot be explained by invoking the average degree of order in the microstructure—without considering further microstructural processes occurring at longer times beyond 3 h—as the parameter controlling the onset of the different phase transitions occurring in this system [21].

### 1.4. Kinetics of the order-disorder transition in Ni–Co–Mn–In alloys

Summarizing, prior results suggested that the kinetics of the

ODO transition may have a significant impact on the final configurational order of the material and, consequently, on its functional properties. Previous works [21,23,24] focused on the effect of the equilibrium degree of order on the MST—arrived at rather quickly according to experiments [24]. However, after the observations of Bruno et al. [32], it is now clear that the overall degree of order present in the samples after heat treatments may be very different from the thermal equilibrium value at the temperature of the SecHT. The origin of this difference may be twofold: either thermal equilibrium stage may not be reached at the end of the isothermal holding stage of the heat treatments, or the system may present significant ordering during post-annealing cooling even if the sample is quenched. The former is more likely to happen at low temperatures since ordering rate may be slow; whereas the later is expected at high temperatures, due to the larger density of vacancies (that facilitates atomic diffusion) and high thermal energy. As a result, the final degree of order in the sample may have a strong dependence on HT temperature, time and cooling rate.

To explore the possible origins of the observed annealing time-dependence of MT properties, it is necessary to analyze the kinetics of ODO process and its dependence on vacancy concentration utilizing a proper theoretical framework, permitting us to evaluate the evolution of the degree of order during typical thermal treatments procedures.

In this work, a more in-depth study of the time evolution of the configurational ordering has been conducted. An *ab initio* based theoretical framework has been proposed to evaluate the kinetics of ODO transitions and the evolution of vacancy concentration. The kinetics of ODO transition in MMSMAs is treated by the vacancy interchange model which considers both nearest neighbor (NN) and second NN atomic jumping within Bragg-Williams-Gorsky (BWG) approximation [37]. It should be mentioned that the concentrations of vacancies are first treated at equilibrium, and then extended to non-equilibrium state where vacancy annihilation process is taken into consideration [38]. Experimental study on  $\text{Ni}_{45}\text{Co}_5\text{Mn}_{50-X}\text{In}_X$  (where X range from 13.4 to 13.6) alloys has also been conducted to investigate the ODO transformation. Both the Curie temperature of the austenite,  $T_C$ , determined using calorimetric measurements, and  $(111)_{L21}$  diffraction peak intensity from the high energy synchrotron measurements were used to monitor the evolution of the degree of  $L2_1$  order. The samples were processed using various heat treatments following four stages: homogenization, initial cooling, secondary HT and final quenching. Finally, comparisons of the computational and experimental results have been presented in what follows.

## 2. Computational methodology

In this section, a variety of computational tools are combined to evaluate the degree of  $L2_1$  order following the workflow depicted in Fig. 1. The equilibrium concentration of vacancies in distinct lattice sites are obtained by *ab initio* predictions using density function theory (DFT) calculations [39,40]. Vacancy diffusion and

annihilation at grain boundaries and dislocation jogs are implemented in non-equilibrium regime calculations [38]. Finally, vacancy concentration calculation is combined with the kinetics model of order-disorder transitions in Heusler alloys to calculate the degree of  $L2_1$  order during ODO transitions [37].

### 2.1. *Ab initio* calculations

The Vienna Atomistic Simulation Package (VASP) was used to perform *ab initio* calculations on an off-stoichiometric  $\text{Ni}_{14}\text{C}-\text{o}_2\text{Mn}_72\text{In}_4$  which is the closest configuration to the experimental condition in a 32-atom special quasirandom structure (SQS). SQS supercells with periodic boundary conditions were employed to evaluate the enthalpy of both bulk and defect structures.

The calculations were performed with Generalized Gradient Approximation (PBE) projector augmented wave pseudopotentials [41] with collinear spin polarization. Integrations in the reciprocal space were obtained over a  $\tau$ -centered Monkhorst-Pack grid in which the number of nodes,  $k$  points, was chosen to be  $N_{kpoint} \approx 5000/N_{atom}$  within the first Brillouin zone [42]. The electronic wave functions were expanded regarding plane waves up to a cutoff kinetic energy of 520 eV. Precision was set to “accurate”. Relaxations were realized using the Hermite-Gauss smearing method of Methfessel and Paxton of order 1, with a smearing parameter of 0.1 eV [43]. The bulk structure was fully relaxed. For the calculations of the defect structures, the volume and shape were kept constant and equal to the ones of the relaxed bulk structure, whereas the ionic positions were relaxed. The convergence criteria for energy was 0.1 meV. All *ab initio* calculations pertain to  $T = 0$  K with zero-point vibrational corrections being neglected. To calculate the vacancy formation enthalpy for  $\text{Ni}_{14}\text{C}-\text{o}_2\text{Mn}_{12}\text{In}_4$ , each kind of atom on a distinct site in the supercell was randomly replaced by a vacancy, giving 5 supercells with a single vacancy and 1 supercell with perfect structure.

### 2.2. Equilibrium vacancy concentration

An SQS supercell approach is utilized to evaluate the equilibrium vacancy concentrations. When generating the SQS structures for the alloys with defects, vacancy is treated as an additional atomic species substituting an atom on the designated lattice site. The vacancy formation enthalpy  $\Delta H_{vac}$  can be extracted from periodic supercell calculations. At  $T = 0$  K, which is typical for *ab initio* calculations, the entropy contribution vanishes so that  $H$  takes the same values as the free energies  $F$ .  $\Delta H_{vac}$  can be derived as below:

$$\Delta H_{vac}(i) = H_{bulk+vac} - H_{bulk} + \mu_i \quad (1)$$

where  $H_{bulk+vac}$  is the defect structure enthalpy which atom  $i$  is vacated,  $H_{bulk}$  is the ground enthalpy of the bulk structure and  $\mu_i$  is the chemical potential of the vacated atom, which is necessary to compensate for the energy balance of the system since the total number of atoms is kept constant. For a pure metal,  $\mu$  is merely the

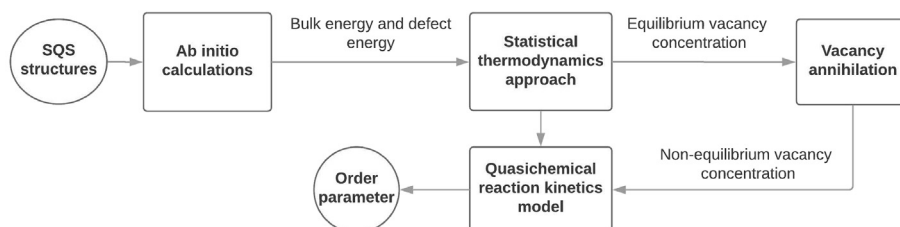


Fig. 1. Flow chart for the theoretical framework to study the ODO process kinetics.

energy of the supercell divided by the number of atoms in it. However, in an off-stoichiometric alloy, the chemical potential of an atomic species could differ from it in the pure metal. The chemical potentials are then calculated by fitting an interpolation formula with respect to composition; details of which can be found in Ref. [39]. The current system is treated as a pseudobinary (Ni–Co)(Mn–In) alloy where each half is treated as a disordered binary alloy [40], i.e. each atom is randomly distributed on the corresponding lattice sites. Henceforth, each of this parts is indicated as sub-binary. If we only consider neighboring pair interactions, a second order polynomial can be used here to describe the enthalpy of each sub-binary alloy system [39]:

$$H_{A-B} = J_0 + x_A J_1 + x_A^2 J_2 \quad (2)$$

where  $x_A$  is the mole fraction of A in A–B alloys;  $J_0$ ,  $J_1$  and  $J_2$  are fitting parameters where  $J_0$  is used to define the enthalpy of pure B,  $J_1$  is used to define the enthalpy of adding element A, and  $J_2$  is used to define the nearest neighbor interactions between A and B. The chemical potential of each species can be extracted from the enthalpy as follows:

$$\begin{aligned} \mu_A(x_A) &= J_0 + J_1 + x_A(2 - x_A)J_2 \\ \mu_B(x_A) &= J_0 - x_A^2 J_2 \end{aligned} \quad (3)$$

The total enthalpy of the general alloy system can be approximated from the average of the enthalpies of the sub-binaries:

$$H_{\text{Ni-Co-Mn-In}} = 0.5H_{\text{Ni-Co}} + 0.5H_{\text{Mn-In}} \quad (4)$$

A list of SQS structures were generated with different compositions which could be divided into two groups. Ni and Co compositions were fixed while Mn and In varied to generate the first half of the SQS structures. Similarly, the second half was generated fixing Mn and In compositions and changing Ni and Co compositions. Chemical potentials  $\mu_i$  could then be extracted from the enthalpy expressions.

In Ni–Co–Mn–In alloy, the vacancy formation enthalpy can be affected by different kinds of atomic species and lattice sites. So the total  $\Delta H_{\text{vac}}$  is the weighted sum over all the species and sites:

$$\Delta H_{\text{vac}} = \sum_{i,p} c_p c_v(i,p) \Delta H_{\text{vac}}(i,p) \quad (5)$$

where  $c_p$  is the site fraction of lattice site  $p$ ,  $c_v(i,p)$  is the vacancy concentration of atom  $i$  on lattice site  $p$  and  $\Delta H_{\text{vac}}(i,p)$  is the vacancy formation enthalpy of atom  $i$  on site  $p$ .

In turn, the vacancy concentration  $c_v(i,p)$  can be expressed as a product of atomic site occupation  $c_i(p)$  and the probability of removing an atom  $i$  from site  $p$ ,  $f_{\text{vac}}(i,p)$ . It is apparent that  $f_{\text{vac}}(i,p)$  should be a function of  $\Delta H_{\text{vac}}(i,p)$  because if the vacancy formation enthalpy is large, the corresponding probability should be low. The vacancy concentration of sub-binary system containing atom A and B can be expressed as follows:

$$c_v(i,p) = c_i(p) \exp\left(-\frac{\Delta H_{\text{vac}}(i,p) + \lambda[\delta_{i,B} x_A - \delta_{i,A} x_B]}{k_B T}\right) \quad (6)$$

where  $\lambda = \Delta H_{\text{vac}}(A) - \Delta H_{\text{vac}}(B)$ ,  $k_B$  is the Boltzmann constant and  $x_{A,B}$  are the mole fractions. The total vacancy concentration on lattice site  $p$  can be obtained from the sum of all the species on that site:

$$c_v(p) = \sum_i c_v(i,p) \quad (7)$$

It can be seen that the effective total vacancy formation enthalpy

may change with respect to temperature. At low temperature, only the site with the lowest formation enthalpy dominates the total distribution, while at high temperature lattice sites with higher  $\Delta H_{\text{vac}}$  also contribute. For the above derivation, we assume that the atomic site occupation is independent of vacancy concentration which can be true in this case where the vacancy concentration is minimal. Due to limited computational resources, we assume that each vacancy only has one local environment while a more comprehensive approach by Zhang et al. [39] indicates that all types of local environments should be taken into account. To compensate for errors, uncertainty is introduced in the following calculations.

### 2.3. Annihilation of vacancy

To expand the equilibrium vacancy states to non-equilibrium conditions, the model assumes vacancy annihilation at grain boundaries and dislocation jogs. For the annihilation at grain boundaries, we assume single grains without internal sources or sinks for vacancies while adjacent grain boundaries are playing the roles of ideal sources and sinks for vacancies.

Then, for instance, when vacancies become supersaturated, they diffuse to the grain boundary to annihilate and results in the vacancy site fraction  $c_v(p)$  reduction until equilibrium vacancy concentration  $c_v^{\text{eq}}(p)$  is reached. The grain is modeled as a sphere with radius  $R$  for simplicity. The equation for the changing rate of vacancy concentration at site  $p$  on grain boundaries  $\dot{c}_v^{\text{GB}}(p)$  is given as [38]:

$$\dot{c}_v^{\text{GB}}(p) = -\frac{15c\tilde{D}_{\text{eq}}}{c_v^{\text{eq}}(p)fR^2} \left( \ln \frac{c_v(p)}{c_v^{\text{eq}}(p)} - \frac{\Omega}{RT} (\sigma_H - \frac{\gamma_b}{R}) \right) \quad (8)$$

For the annihilation at dislocation jogs, we consider a unit volume crystal with jog density  $H$  and the equation for the changing rate of vacancy concentration at site  $p$  on jogs  $\dot{c}_v^{\text{DJ}}(p)$  [38]:

$$\dot{c}_v^{\text{DJ}}(p) = -\frac{2\pi a H c_v(p) \tilde{D}_{\text{eq}}}{c_v^{\text{eq}}(p)f} \left( \ln \frac{c_v(p)}{c_v^{\text{eq}}(p)} - \frac{\Omega}{R_g T} \sigma_H \right) \quad (9)$$

Where in the two equations above,  $c_v^{\text{eq}}$  is the equilibrium vacancy concentration;  $f$  is the geometrical correlation factor for BCC;  $\tilde{D}_{\text{eq}}$  is the interdiffusion coefficient which equals to  $\frac{1}{6}a^2\nu \exp\left(-\frac{H_m}{RT}\right)$ , in which  $a$  is the lattice parameter (taken from Ref. [44]),  $\nu$  is the vacancy attempt frequency, and  $H_m$  is the vacancy migration energy;  $R$  is the grain size;  $\Omega$  is molar volume;  $R_g$  is gas constant;  $\sigma_H = 0$  is the hydrostatic stress;  $\gamma_b$  is grain boundary energy. The values of parameters are shown in Table 1.

### 2.4. Kinetics of B2-L2<sub>1</sub> ordering

The kinetics of L2<sub>1</sub> ordering is analyzed through a quasichemical reaction model taking into account the interchanges of atoms with vacancies within the BWG approximation. The unit cell of the studied structures can be split in different sublattices,  $X^*$  and  $Y^*$  for B2 and X, Y and Z for L2<sub>1</sub>, where Y and Z correspond to a breaking of the symmetry in the site occupancy of the  $Y^*$  sublattice. In the off-stoichiometric Ni<sub>14</sub>Co<sub>2</sub>Mn<sub>12</sub>In<sub>4</sub> alloys, sublattice  $X^*$  (X) of phases B2 (L2<sub>1</sub>) is preferably occupied by Ni and Co atoms with no internal ordering. Therefore, it is useful to define an effective atom Ni\* which consists of 87.5% Ni and 12.5% Co, simplifying numerical calculations. In general, the site occupancies of Ni\*, Mn, In and vacancy on site  $p$  ( $p = X, Y, Z$ ) can be denoted as  $c_{\text{Ni}^*}(p)$ ,  $c_{\text{Mn}}(p)$ ,



**Table 1**

Values of parameters used in the simulation.

f	$H_m$ (J/mol)	$\nu$ ( $s^{-1}$ )	a (Å)	R ( $\mu\text{m}$ )	$\gamma_b$ (J/m <sup>2</sup> )	H ( $m^{-1}$ )
0.72	$1.3 \times 10^5$	$1 \times 10^{13}$	3.03	10	0.10	$6.90 \times 10^4$
$\Omega$ (m <sup>3</sup> /mol)	$V_{Ni^*,Ni}$ (K)	$V_{Mn,Mn}$ (K)	$V_{In,In}$ (K)	$U_1$ (K)	$U_2$ (K)	$\nu_k$ (s <sup>-1</sup> )
$8.41 \times 10^{-6}$	-5171.01	-6700	-1241.28	6500	6500	$3 \times 10^{10}$

$c_{In}(p)$ ,  $c_v(p)$  respectively [37].

Given that the order-disorder transition between B2 and L2<sub>1</sub> in the present system results from the symmetry breaking of Y\* into Y and Z, the possible atomic concentrations in B2 for Y and Z in the present alloy system can be written as a function of the mole fractions  $x$  as:

$$c_{Mn}(Y) = c_{Mn}(Z) = 2x_{Mn}; c_{In}(Y) = c_{In}(Z) = 2x_{In} \quad (10)$$

while for L2<sub>1</sub> one need to take into account that the system is off-stoichiometric,  $x_{Mn} > 0.25$ , and that Y and Z are computationally equivalent:

$$c_{Mn}(Y) = 1; c_{Mn}(Z) = 4x_{Mn} - 1; c_{In}(Y) = 0; c_{In}(Z) = 4x_{In} \quad (11)$$

$$c_{Mn}(Y) = 4x_{Mn} - 1; c_{Mn}(Z) = 1; c_{In}(Y) = 4x_{In}; c_{In}(Z) = 1 \quad (12)$$

Then, one can define an order parameter,  $S_{L2_1}$ , such that its value ranges between 0 (B2) and 1 (L2<sub>1</sub>) as:

$$S_{L2_1} = \frac{1}{2} \left( \frac{c_{Mn}(Y) - 2x_{Mn}}{1 - 2x_{Mn}} + \frac{c_{In}(Z) - 2x_{In}}{2x_{In}} \right) \quad (13)$$

The quasichemical reactions for the interchange of vacancies with 1st and 2nd NN atoms can be expressed as follows:



with reaction rates from left to right derived as follows:

$$R_{nip} = 2N\nu_1 [c_i(X)c_v(p)\exp\{- (U_1 + Q_{nip})/2T\} - c_v(X)c_i(p)\exp\{- (U_1 - Q_{nip})/2T\}] \quad (15.1)$$

$$R_{mi} = 1.5N\nu_2 [c_i(Y)c_v(Z)\exp\{- (U_2 + Q_{mi})/2T\} - c_v(Y)c_i(Z)\exp\{- (U_2 - Q_{mi})/2T\}] \quad (15.2)$$

where  $i = Ni^*, Mn$  or  $In$ ,  $p = Y$  or  $Z$ ,  $N$  is the number of lattice points,  $\nu_1$  and  $\nu_2$  are the attempt frequency and  $U_1$  and  $U_2$  are the height of potential barriers for the vacancies interchange with atoms between 1st NN and 2nd NN, respectively.  $T$  is temperature,  $Q_{nip}$  and  $Q_{mi}$  are changes of the configurational energy due to quasichemical reactions. The vacancy site fractions are obtained from Section 2.2 and 2.3.  $Q_{nip}$ ,  $Q_{mi}$  are given as below:

$$Q_{NiY,i=Ni^*,Mn,In} = \sum_{j=Ni^*,Mn,In} [V_{ij}(7c_j(X) - 3c_j(Y) - 4c_j(Z)) - 6W_{ij}(c_j(X) - c_j(Z))] \quad (16.1)$$

$$Q_{NiZ,i=Ni^*,Mn,In} = \sum_{j=Ni^*,Mn,In} [V_{ij}(7c_i(X) - 3c_j(Z) - 4c_j(Y)) - 6W_{ij}(c_i(X) - c_j(Y))] \quad (16.2)$$

$$Q_{mi,i=Ni^*,Mn,In} = 5 \sum_{j=Ni^*,Mn,In} [W_{ij}(c_j(Y) - c_j(Z))] \quad (16.3)$$

where  $V_{ij}$  and  $W_{ij}$  indicate the energy of atom  $i$  and  $j$  pair in the first NN and second NN. Note that there are six first NN reactions in Eq. (14.1), corresponding to  $R_{nip}$ , while there are three second NN reactions in Eq. (14.2), for  $R_{mi}$ .

The evolution rate of the  $S_{L2_1}$  long range parameter is described using the rate of quasichemical reactions as follows:

$$\frac{dS_{L2_1}}{dt} = \frac{4}{N} \left( 2[R_{nMnY} - R_{mMn}] + \sum_{i=Ni^*,In} [R_{mi} - R_{niY}] \right) + \frac{2}{N} \left( 2[R_{nInZ} + R_{mIn}] - \sum_{i=Ni^*,Mn} [R_{mi} + R_{niZ}] \right) \quad (17)$$

To solve this differential equation, a numerical ODE solver was utilized with adaptive time stepping. By integrating the differential equations simultaneously in this section and above two sections, the kinetic behavior of L2<sub>1</sub> and B2 ordering in the Ni<sub>14</sub>Co<sub>2</sub>Mn<sub>12</sub>In<sub>4</sub> Heusler alloy can be analyzed and the degree of L2<sub>1</sub> order can be derived. A more detailed description of this methodology can be found in Ref. [37].

This method requires to estimate the effective bonding energies between  $ij$  pairs in the first NN,  $V_{ij}$ , and second NN,  $W_{ij}$ , being  $i, j = Ni^*, Mn$  or  $In$ . Firstly, when  $i = j$ , it has been assumed that the energy between the 2nd NN are one half of that between 1st NN pairs,  $V_{ii} = 2W_{ii}$ . Secondly,  $V_{ii}$  has been calculated from their relationship with the vacancy formation energy,  $E_v^F(i) = -\frac{1}{2}ZV_{ii}$ , where  $Z$  is the coordination number [45].  $E_v^F(i)$  are obtained from *ab initio* calculations of pure Ni, Co, Mn or In BCC structures while  $E_v^F(Ni^*)$  is taken to be the weighted average of 87.5%  $E_v^F(Ni)$  and 12.5%  $E_v^F(Co)$ , resulting in  $V_{Ni^*,Ni^*}$ ,  $V_{Mn,Mn}$  and  $V_{In,In}$  shown in Table 1. Thirdly, when  $i \neq j$ , the effective bonding energies are calculated from the corrected average of the  $V_{ii}$  terms as:

$$V_{ij,i \neq j} = \frac{1}{2} \sum_{k=i,j} V_{kk} - V_{ij}^\dagger \quad (18.1)$$

$$W_{ij,i \neq j} = \frac{1}{2} \sum_{k=i,j} W_{kk} - W_{ij}^\dagger \quad (18.2)$$

where  $V_{ij}^\dagger$  and  $W_{ij}^\dagger$  are the correction terms, which increases the strength of the bonds when positive. In the quaternary Ni<sub>14</sub>Co<sub>2</sub>Mn<sub>12</sub>In<sub>4</sub> alloys, sublattice X should be preferably occupied by Ni\* atoms in both phases, L2<sub>1</sub> and B2. Therefore, bonds occurring when Ni\* is in the Y or Z sublattices or when Mn or In are in the X sublattice can be assumed to be relatively easy to break. Then, we made  $V_{MnIn}^\dagger = W_{Ni^*,Mn}^\dagger = W_{Ni^*,In}^\dagger = 0$  K for the sake of simplicity. In its turn, the values of  $V_{Ni^*,Mn}^\dagger$ ,  $V_{Ni^*,In}^\dagger$  and  $W_{MnIn}^\dagger$  were chosen so that  $S_{L2_1}$  is around 0.1 when the sample is close to the experimental ODO

temperature ( $\approx 900$  K [15]). This arbitrary value was chosen to avoid numerical instability occurring at the degree of order 0. However, a range of values was used instead of a single value in order to account for the uncertainty in the kinetics model, for which  $900 \leq V_{\text{Ni-Mn}}^{\ddagger} \leq 1000$  K,  $500 \leq V_{\text{Ni-In}}^{\ddagger} \leq 550$  K and  $650 \leq W_{\text{MnIn}}^{\ddagger} \leq 680$  K.

Lastly, the frequency factors,  $\nu_1 = \nu_2 = \nu_s$  and the potential energy barriers for vacancy interchange,  $U_1$  and  $U_2$ , are shown in Table 1. Energy barriers were obtained by Nudged Elastic Band (NEB) calculations which is a method to find saddle points and minimum energy paths between different lattice sites. The calculations were carried out by VASP-vtst version with the direct jump and 6-step jump of Mn and In atoms.

### 3. Experimental techniques

#### 3.1. Curie temperature

In Ni–Mn-based MMSMAs, the Curie temperature of the austenite,  $T_C$ , displays a strong monotonic dependence on the overall degree of  $L2_1$  atomic ordering [46]. Therefore,  $T_C$  has been employed to indirectly explore the dependence of the degree of order on the thermal procedure for both  $L2_1$  and B2 ordering processes.

For this purpose, two sets of  $\text{Ni}_{45}\text{Co}_5\text{Mn}_{36.4}\text{In}_{13.6}$  polycrystalline samples were prepared following the heat treatment schedules illustrated in Fig. 2. Both sets were homogenized at 1173 K for 24 h, and cooled down to room temperature using two different cooling rates. The first set was water quenched (WQ samples) in order to retain a significant amount of B2 phase, while the second set was cooled in the furnace (FC samples) with a controlled cooling rate of 0.00463 K/s (from 1173 to 373 K in 48 h), which should lead to a high degree of  $L2_1$  order. Selected samples from each set were then subjected to secondary heat treatments at temperatures ranging from 673 to 773 K, and for durations ranging from 0.25 to 24 h, followed by water quenching, in order to retain the degree of order. A TA Instruments Differential Scanning (DSC) was used to determine  $T_C$ s as the inflection point in the heat flow curve during the heating and cooling cycles, generated by the ferromagnetic transition.  $T_C$  results were averaged over two cooling-heating cycles.  $T_C$  was also determined as the inflection point in the thermomagnetization curves under low magnetic fields, generated using a Quantum Design superconducting magnetometer for most of the

samples in order to validate the DSC results. Differences in  $T_C$  determined using two different methods were  $< 2$  K and  $T_C$ s from both methods followed the same trend with temperature and duration of the secondary heat treatments.

#### 3.2. High energy XRD measurements

A single crystal bar of  $\text{Ni}_{45}\text{Co}_5\text{Mn}_{36.6}\text{In}_{13.4}$  (nominal composition) was first homogenized at 1173 K for 24 h and water quenched. Transmission X-Ray Diffraction experiments were conducted at the Advanced Photon Source, Argonne National Laboratory (Lemont) using the high-energy synchrotron radiation with wavelength 0.1173 Å. In order to mimic the evolution of the configurational order during conventional heat treatments, the samples were heated at 50 K/min from room temperature to different temperatures between 673 K and 773 K and held at the temperature isothermally. During this process, polar diffraction patterns were obtained in regular time-steps. Finally, the time-evolution of the overall degree of order was estimated integrating the diffracted intensity corresponding to the [111] direction of the austenite cubic phase, which is the characteristic signature of the  $L2_1$  ordered phase [26,47,48].

### 4. Results

The calculated equilibrium concentration of vacancies,  $c_v^{eq}$ , for  $\text{Ni}_{14}\text{Co}_2\text{Mn}_{12}\text{In}_4$  at different lattice sites of the Heusler structure,  $L2_1$  phase, and of the B2 phase are shown in Fig. 3. Note that Y and Z sites of  $L2_1$  are integrated into  $Y^*$  of the B2 phase, which is occupied indistinctly by Mn and In atoms because of B2's higher symmetry. This figure shows that, for both phases, equilibrium vacancy concentration in the  $\text{Ni}^*$  sites, X or  $X^*$ , is much higher than in the sites occupied by Mn and In atoms. This fact suggests that the diffusion of Mn and In atoms should be mediated mostly by the 1st NN vacancies on the  $\text{Ni}^*$  sites, which is in good agreement with the assumption that vacancy assisted atomic diffusion is the main mechanism driving the ODO process.

In what follows, we attempt to describe the atomistic mechanisms and the governing kinetics of the ODO transition during typical thermal treatments, Fig. 2, and establish correlations

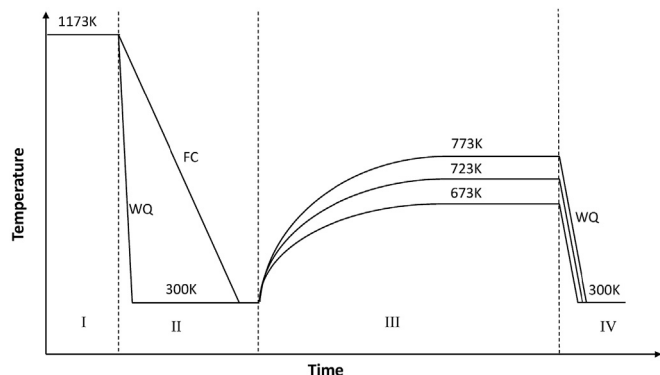


**Fig. 2.** Heat treatment schedules applied to  $\text{Ni}_{45}\text{Co}_5\text{Mn}_{36.4}\text{In}_{13.6}$  MMSMA to investigate the kinetics of the degree of  $L2_1$  ordering. Step (I) is high-temperature homogenization at 1173 K. (II) is the initial cooling process composed either of fast water quenching or slow furnace cooling. (III) is the heating and isothermal holding processes at different temperatures for achieving different degrees of order. (IV) is the final quenching step to retain the degree of order.

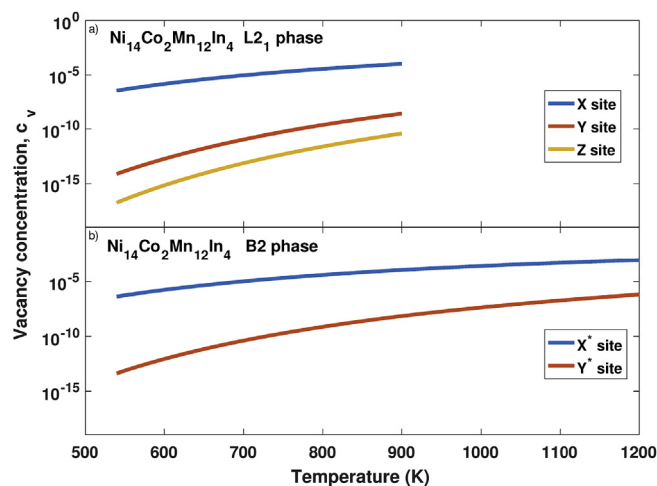


**Fig. 3.** Calculated equilibrium vacancy concentration of  $\text{Ni}_{14}\text{Co}_2\text{Mn}_{12}\text{In}_4$  for (a)  $L2_1$  and (b) B2 phase. For (a), X site, blue, is occupied by Ni and Co, Y site, red, is occupied by Mn and Z site, yellow, is occupied by Mn and In. For (b),  $X^*$  site, blue, is occupied by Ni and Co while  $Y^*$  site, red, is occupied by Mn and In. (For interpretation of the references to colour in this figure legend, the reader is referred to the Web version of this article.)

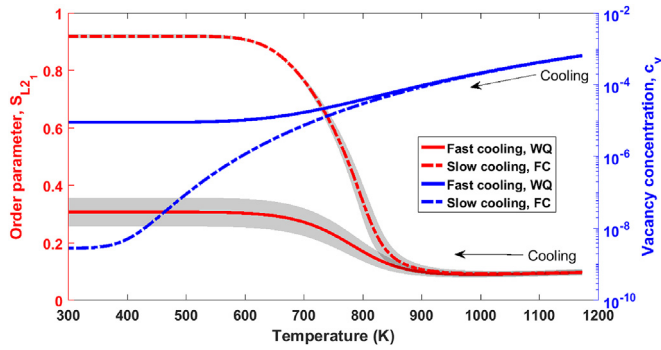


**Fig. 4.** Calculated degree of  $L_{21}$  order, in red, and vacancy concentration, in blue, during cooling to 300 K from 1173 K with the rates of  $-100$  K/s, WQ protocol, solid lines, and  $-0.01$  K/s for the FC protocol, dashed lines, for  $\text{Ni}_{14}\text{Co}_2\text{Mn}_{12}\text{In}_4$ . Gray shadows represent the estimated uncertainty from the selection of  $V_{\text{Ni-Mn}}^i$ ,  $V_{\text{Ni-In}}^i$  and  $W_{\text{MnIn}}^i$  values. Note that y-axis is linear for order parameter and logarithmic for the vacancy concentration. (For interpretation of the references to colour in this figure legend, the reader is referred to the Web version of this article.)

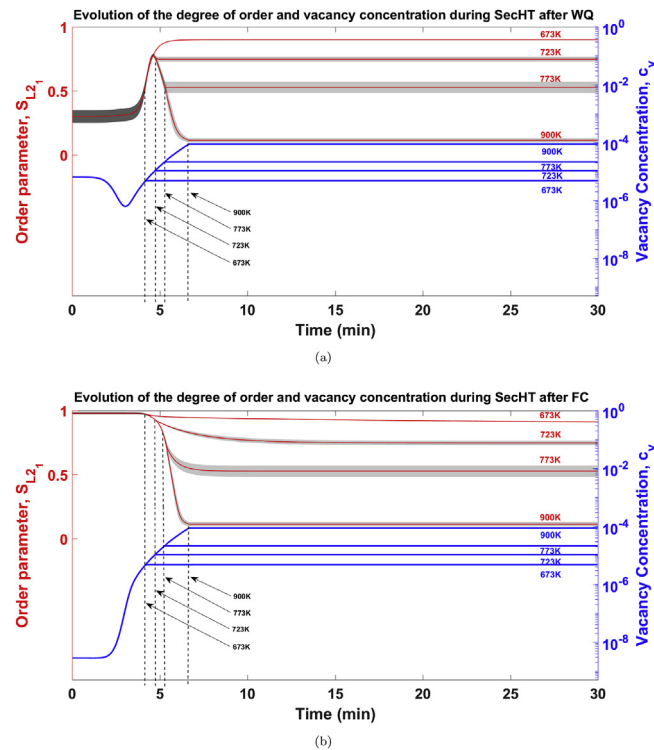


**Fig. 5.** Calculated degree of  $L_{21}$  order, red, and vacancy concentration, blue, during annealing at different temperatures after Water Quench (a) and Furnace Cool (b) from 1173 K to room temperature. Shadows are the confident range considering  $V_{\text{Ni-Mn}}^i$ ,  $V_{\text{Ni-In}}^i$  and  $W_{\text{MnIn}}^i$  uncertainty. (For interpretation of the references to colour in this figure legend, the reader is referred to the Web version of this article.)

between the resulting ordering state and the characteristics of  $\text{Ni}_{14}\text{Co}_2\text{Mn}_{12}\text{In}_4$  ferromagnetic and martensitic transitions. To achieve this, one first requires to accurately describe the vacancy generation/annihilation to understand the kinetics of the ODO transition. Therefore, the evolution of vacancy concentration,  $c_v$ , and order parameter,  $S_{L_{21}}$ , at different stages of the thermal procedure is shown in Figs. 4–6.

To begin with, stage I in Fig. 2 represents the homogenization of the material at temperatures above the B2– $L_{21}$  order-disorder transition and stage II consist on the initial cooling process

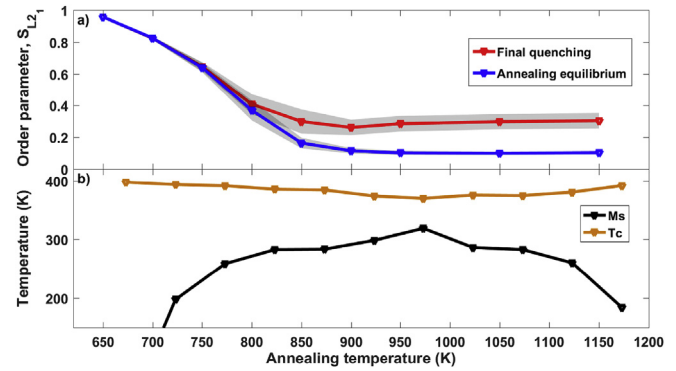


**Fig. 6.** (a) Calculated  $S_{L_{21}}$  with respect to different SecHT temperatures for a  $\text{Ni}_{14}\text{Co}_2\text{Mn}_{12}\text{In}_4$  alloy. The blue curve is  $S_{L_{21}}^{\text{eq}}$ , which is in pre-quenching thermal equilibrium state. The red curve is  $S_{L_{21}}^{\text{quenched}}$ , which is after quenching from thermal equilibrium state. Gray shadows represent the estimated uncertainty from selection of  $V_{\text{Ni-Mn}}^i$ ,  $V_{\text{Ni-In}}^i$  and  $W_{\text{MnIn}}^i$  values. (b) Experimental  $T_c$ , brown, and  $M_s$ , black, temperatures for a polycrystalline  $\text{Ni}_{45}\text{Co}_5\text{Mn}_{36.4}\text{In}_{13.6}$  alloy.  $M_s$  falling below the bottom axis indicates that the sample did not show MT (transformation arrest). (For interpretation of the references to colour in this figure legend, the reader is referred to the Web version of this article.)

between 1173 K and room temperature. Fig. 4 presents the temperature dependence of  $c_v$  and  $S_{L_{21}}$  during stage II using two different cooling rates, where Water Quenching (WQ) correspond to a typical uncontrolled fast cooling, the rate of which was chosen to be  $-100$  K/s for the numerical calculations, while Furnace Cooling (FC) stands for a controlled slow cooling ( $-0.01$  K/s). The last rate is rounded to the closest digit for model simplicity. The curves start at the high-temperature side of the figure, corresponding to the end of stage I where the material is expected to be highly disordered. This figure shows that WQ was able to retain a significant amount of high-temperature vacancies and disorder at room temperature. In comparison, during FC, there was more time for the diffusion of atoms and vacancies leading to a much higher degree of  $L_{21}$  ordering at room temperature. It is significant that even for the controlled slow cooling the final ordering is not the absolute maximum, 1, and that the curves in Fig. 4 are flat below certain temperature: 600 K for  $S_{L_{21}}$  and 400 K for  $c_v$ . Calculations thus predict that there is a practical maximum achievable degree of order, which is a consequence of the sluggish kinetics at low temperature.

The same methodology has been employed to calculate the evolution of the ODO transition during stage III of Fig. 2, which consist of the heating and isothermal sections of standard secondary heat treatments at temperature: 673 K, 723 K, 773 K or 900 K. Fig. 5 presents the evolution of  $c_v$  and  $S_{L_{21}}$  during these secondary heat treatments for samples with two different initial conditions as set from the different cooling rates during stage II: WQ samples and FC samples. Other than the initial conditions, the thermal procedures followed in Fig. 5a and b are identical.

As introduced above, these figures contain two well-differentiated stages: heating and isothermal hold stages. During the first stage, starting at  $t = 0$  s, the material is heated at 1.5 K/s from 300 K to the SecHT temperature, which is different for each case and thus reached at different times (indicated by the dashed lines). Note that the heating rate used, 1.5 K/s, is a conservative value selected in order to imitate the common thermal procedures without underestimating the time required for the sample to reach furnace's temperature. In turn, the second stage consists of holding the material isothermally at 673 K, 723 K, 773 K or 900 K for time large enough to reach equilibrium levels of  $c_v$  and  $S_{L_{21}}$ .

In Fig. 5a, at the beginning of the heating process,  $c_v$  and  $S_{L_{21}}$  are

time-independent since the kinetics is slow at such low temperature regime. Next, atomic diffusion “unfreezes” with further increase of the temperature, starting the vacancy annihilation and ordering processes. Note here that current heating rate, 1.5 K/s, is slower than the initial fast cooling,  $-100$  K/s. So, when atomic diffusion is “unfrozen”, the vacancy concentration and the degree of  $L_{21}$  ordering tends to approach their equilibrium levels at such temperature. For this reason, the first tendency observed during heating is to annihilate the vacancies, decreasing  $c_v$ , and increase  $L_{21}$  ordering. Following heating the samples, an inflection point is reached because the current level of  $c_v$  and  $S_{L_{21}}$  reaches its equilibrium values at such temperature. Then, kinetics is fast enough to keep  $c_v$  and  $S_{L_{21}}$  in their thermal equilibrium values for the rest of the heating stage. Note that  $c_v^{eq}$  increases with  $T$  while  $S_{L_{21}}^{eq}$  decreases. Also, note that the curve for  $S_{L_{21}}$  for the heat treatment at 673 K in the only one not showing an inflection point. For the particular initial condition of Fig. 5a and 673 K is achieved on heating before  $S_{L_{21}}$  reaches  $S_{L_{21}}^{eq}$ . Then, the sample enters into the isothermal stage with some quenched-in disorder and requires few minutes to reach thermal equilibrium. On the contrary, samples heated to 723 K, 773 K or 900 K have reached thermal equilibrium in the inflection point, before arriving at the SecHT temperature. Therefore, they do not evolve during the isothermal stage, presenting a flat line. The same can be applied for the concentration of vacancies, only changing that the inflection point, and thus  $c_v^{eq}$ , is reached at a lower temperature, and therefore all samples are stable during the isothermal stage.

In Fig. 5b, the material starts from a minimum of quenched-in vacancies and disorder. Contrary to the previous case, the initial cooling rate is much lower,  $-0.01$  K/s. Then, when atomic diffusion is “unfrozen” during heating, the thermal equilibrium concentration of vacancies and disorder are higher than the current levels of  $c_v$  and  $S_{L_{21}}$ , the opposite of what is reported in Fig. 5a. Since the  $c_v$  and  $S_{L_{21}}$  and their equilibrium values present the same tendency along the entire heating, there is no inflection point and the time at which the variables reach their equilibrium levels is not evident. For the vacancy concentration, the thermal equilibrium is reached before 673 K since the isothermal stages are shown as flat lines without any evolution after abandoning the heating stage. On the other hand, 673 K, 723 K, and 773 K curves for  $S_{L_{21}}$  present transitory decay to their  $S_{L_{21}}^{eq}$  levels when heating is interrupted. This evolution during the isothermal stage can get to last about 10 min and points out that  $S_{L_{21}}$  only reach  $S_{L_{21}}^{eq}$  on heating above 773 K. Significantly, calculations have shown that i) the equilibrium levels of  $c_v$  and  $S_{L_{21}}$  are reached within the first 15 min of the annealing process in all cases, which is faster than suggested by previous, but indirect, results [32], and ii) since  $c_v^{eq}$  and  $S_{L_{21}}^{eq}$  only depend on temperature, short heat treatments should lead to the same values of vacancy concentration and overall degree of order independently of the initial state.

The final stage of the thermal procedure, stage IV on Fig. 2, consists of the cooling process from the secondary heat treatment temperature to 300 K. Usually, the samples are water quenched in an attempt to retain the degree of order at the SecHT temperatures, being able this way of tuning the characteristics of the MT, e.g. Refs. [21,32]. However, during this cooling process, the samples stay briefly within a temperature range that permits atomic diffusion. Therefore, as seen above for the fast cooling from 1173 K in Fig. 4, it is expected that some vacancy annihilation and ordering occur leading to a final order state at room temperature different from the pre-quenching thermal equilibrium state. This difference has also been investigated using numerical simulations. First, the initial

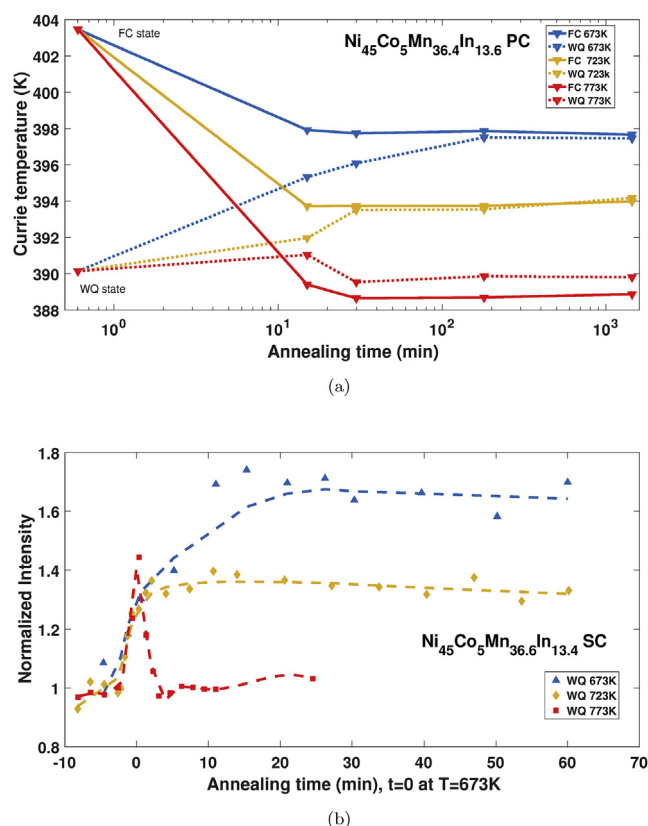
states of the samples correspond to the end of stage III (Fig. 5), where they are at thermal equilibrium for the different SecHT temperatures. Then, the material is fast cooled,  $-100$  K/s, from the annealing temperature to 300 K.

Fig. 6a shows the heat treatment temperature dependence of  $S_{L_{21}}^{eq}$  and of the degree of order after fast cooling,  $S_{L_{21}}^{quenched}$ . Note that the difference between these two curves represents the ordering occurred during the fast cooling process,  $S_{L_{21}}^{cooling}$ . For temperatures below 700 K,  $S_{L_{21}}^{eq}$  and  $S_{L_{21}}^{quenched}$  coincides, meaning that  $S_{L_{21}}^{cooling}$  is negligible since kinetics is slow. However,  $S_{L_{21}}^{eq}$  and  $S_{L_{21}}^{quenched}$  diverge on increasing the heat treatment temperature as atomic diffusion becomes fast enough to produce ordering during the fast cooling. With further increase of SecHT temperature,  $S_{L_{21}}^{eq}$  stabilizes above ODO temperature, representing that the transition to B2 phase is complete, while  $S_{L_{21}}^{quenched}$  presents a minimum near the ODO temperature. This minimum is the result of  $S_{L_{21}}^{eq}$  and  $S_{L_{21}}^{cooling}$  having an opposite dependence on the SecHT temperature. The increase of the SecHT temperature enhances the available thermal energy and the density of vacancies, both accelerating atomic diffusion. Consequently,  $S_{L_{21}}^{cooling}$  increases with SecHT temperature both below and above the ODO temperature. In summary, below the minimum of  $S_{L_{21}}^{quenched}$ , the negative temperature dependence of  $S_{L_{21}}^{eq}$  is the major contributor to the change in  $S_{L_{21}}^{quenched}$  as kinetics is fairly slow. Above this minimum, the positive temperature dependence of  $S_{L_{21}}^{cooling}$  is dominant since the equilibrium state of the material is in fully B2 regardless of SecHT temperature. The reason why this minimum is near the ODO temperature is that the negative temperature dependence of  $S_{L_{21}}^{eq}$  is notably stronger than the positive temperature dependence of  $S_{L_{21}}^{cooling}$  below ODO temperature.

One can relate the predicted minimum of the SecHT temperature dependence of  $S_{L_{21}}^{quenched}$  with experimental results on any property with a significant dependence on the  $L_{21}$  overall degree of order, like the critical temperatures of the ferromagnetic transition in the austenite,  $T_C$  [49], and the martensitic transformation,  $M_S$  [47]. Fig. 6b presents the heat treatment temperature dependence of  $T_C$  and  $M_S$  for polycrystalline  $Ni_{45}Co_5Mn_{36.4}In_{13.6}$  (nominal composition) samples which were heat treated following the WQ path in Fig. 2. Both characteristic temperatures present a non-monotonic dependence with SecHT temperature (a minimum for  $T_C$  and a maximum for  $M_S$  at 973 K), which is related to the non-monotonic behavior of the experimental  $S_{L_{21}}^{quenched}$ . The same behavior was observed in similar alloy systems like Ni–Mn–Ga [27] and Ni–Fe–Ga [50]. Therefore, these observations reinforce the validity of the numerical calculations presented in this work.

After predicting the unusual—in light of previous assumptions and results by Monroe et al. [21] and Bruno et al. [32]—fast kinetic process of ODO transition from the simulations, further experiments were conducted as an effort to verify the predictions. The correlation between  $T_C$ , Fig. 6, and the overall degree of order has been employed to estimate the dependence of  $S_{L_{21}}^{quenched}$  on the duration of annealing treatments. Fig. 7a presents the annealing time dependence of the Curie temperature for  $Ni_{45}Co_5Mn_{36.4}In_{13.6}$  samples with different initial conditions, either WQ or FC. This figure can be compared with Fig. 5 as both experimental  $T_C$  and calculated  $S_{L_{21}}$  start at the low level for WQ samples and high level for FC samples, and during the annealing, they tend to reach a value that depends on SecHT temperature. Again, the higher the SecHT temperature is, the lower the fraction of  $L_{21}$  phase of the





**Fig. 7.** (a) Experimental measurements of the Curie temperatures for the samples annealed at 673 K (blue), 723 K (yellow) or 773 K (red) after either WQ (solid lines) or FC (square-dashed lines) thermal procedures for polycrystalline  $\text{Ni}_{45}\text{Co}_5\text{Mn}_{36.4}\text{In}_{13.6}$  alloy. (b) Normalized  $(111)_{L21}$  peak intensity, where  $I(\text{WQ state}) = 1$ , for the  $\text{Ni}_{45}\text{Co}_5\text{Mn}_{36.6}\text{In}_{13.4}$  single crystal WQ samples heated to 673 K (blue), 723 K (yellow) or 773 K (red) and held isothermally. Long-dashed lines are guides for the eyes. (For interpretation of the references to colour in this figure legend, the reader is referred to the Web version of this article.)

equilibrium state should be. Interestingly,  $T_C$  for the FC samples seems to be almost annealing time-independent, since most of the change in  $T_C$  between the initial FC state and the after-annealed ordering states occurred within the first 15 min of SecHT. Curiously, WQ samples seem to require more time to reach a stable  $T_C$  level. This difference may suggest an asymmetry between the ordering and disordering processes not predicted by the calculations.

A second way to estimate the evolution of the overall degree of order during the thermal processing is by means of monitoring the characteristic diffraction peaks of the  $L_{21}$  structure in-situ on X-ray diffraction. In particular, Fig. 7b shows the in-situ measurements of the intensity (normalized area of the peak) of the  $(111)$  diffraction peak for WQ samples heated at 50 K/min to different temperatures and then held isothermally. Now, the comparison of the experiments with Fig. 5a is very direct since the in-situ evolution of the order parameter was determined and not its after-quench state like in 7a. It should be emphasized that the sample heated to 773 K exhibited the same inflection point that was predicted by the calculations, Fig. 5, which occurs when, thanks to the rapid nature of the ODO kinetics,  $S_{L21}$  reaches  $S_{L21}^{eq}$  in the middle of the heating process. Therefore, the in-situ high energy XRD experiments suggest that thermal equilibrium overall degree of order is reached within the first 15 min for WQ samples, as predicted by the calculations. The time required to reach  $S_{L21}^{eq}$  for both ordering and disordering processes is similar, and then, the differences observed

between the  $T_C$  of WQ and FC samples need to be as a result of another mechanism affecting  $T_C$ , which may be the topic for future work.

## 5. Discussion of the results

Computational and experimental results in this work show the dependence of the ordering rate, as the time-evolution of the overall order parameter, on the vacancy concentration and temperature. Besides, the investigation of the ODO kinetics permitted us to determine the evolution of the overall degree of order through different common thermal procedures.

To begin with, the ordering process has a strong dependence on the SecHT temperature. Below 600 K, the kinetics is slow enough for the system to be considered as “frozen” within the experimental time-scale window. In this way, Fig. 4 shows that the ordering stop increasing below 600 K even with a cooling rate as low as 0.01 K/s. Consequently, fully ordered state ( $S_{L21} = 1$ ) can't be reached in a reasonable amount of time. On the other hand, above 600 K, Fig. 5 demonstrates that the system requires short periods of time for the overall degree of order to reach its thermal equilibrium level,  $S_{L21}^{eq}$ . Furthermore, Fig. 5a shows that, for the given heating rate, 1.5 K/s, and initial  $S_{L21}$ , the system can get to thermal equilibrium during heating so that it remains time-independent during the subsequent heat treatment isothermal holding. This fact was corroborated by in-situ transmission high energy XRD experiments, Fig. 7b. Typically, secondary heat treatments have a duration no shorter than 15 min [31,32] and are performed at temperatures similar to or higher than 600 K [21]. Therefore, one can assume that the  $S_{L21}^{eq}$  was achieved during most of the isothermal heat treatments present in the literature.

Although the thermal equilibrium is very likely reached during isothermal holding,  $S_{L21}$  is again out of equilibrium once the material starts to be cooled down to room temperature. Fig. 4 shows that there is a competition between the ordering rate and the cooling rate since high cooling rates can quench-in part of the disorder and vacancies. However, Fig. 6 indicates that the disorder can only be effectively retained below 800 K. Above this temperature, Fig. 6 points out that the ordering attained on cooling from the ODO transition temperature could hardly be negligible even for the highest quenching rates. Furthermore, the higher SecHT temperature increases the vacancy concentration, accelerating the ODO transition during cooling. This fact explains the minimum of  $S_{L21}^{quenched}$  when the material is heat treated close to its ODO transition temperature.

The impact of these facts on the experimental results reported in the literature is varied. First, it is not experimentally possible to have samples at room temperature without a certain degree of order, since ODO transition is too fast above 800 K to be prevented, regardless of the quenching rate. Therefore, despite the fact that some thermal treatments were designed to maximize/minimize the degree of ordering in previous works, see for example [25,31], these samples cannot be ascribed to either B2 or  $L_{21}$  phases, but a mixed state. In general, the degree of ordering of this mixture is defined by the SecHT temperature, cooling rate and, within a narrow range of HT temperatures around 600 K, on SecHT duration. However, in most cases the final overall degree of order can be adequately considered as SecHT duration independent.

It is important to note that a specific overall degree of order,  $S_{L21}$ , does not correspond to a single configuration of the ordering domains. On the one hand, since ODO process is a second-order transformation, change in long-range order parameter should occur by successive local rearrangements which occur

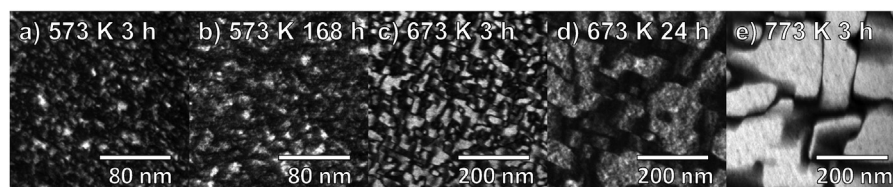


**Fig. 8.**  $[111]_{L2_1}$  dark-field micrographs collected in the (011) cubic austenite zone axis for  $\text{Ni}_{45}\text{Co}_5\text{Mn}_{36.6}\text{In}_{13.4}$  single crystal WQ samples that were secondary heat treated and different temperature during different times: (a) 573 K 3 h, (b) 573 K 168 h, (c) 673 K 3 h, (d) 673 K 24 h and (e) 773 K 3 h. Note that samples annealed at 573 K, (a) and (b), are shown with a different magnification than (c)–(e). These micrographs were published in Ref. [32] and they are reproduced here with permission.

homogeneously throughout the entire crystal. These successive rearrangements should lead to a continuous series of intermediate states which progressively increases the stability of the system until the  $L2_1$  ordered domains can be formed. As introduced above, the ODO transition cannot be completed during cooling even for low cooling rates, and then it always is partially quenched. As a consequence,  $L2_1$  ordered domains contain internal disorder in the form of ordering defects, anti-sites and vacancies. On the other hand, the lattice can break the B2 phase symmetry into two equivalent ordering variants, two  $L2_1$  anti-phase domains, during the initial local rearrangements. This process can necessarily produce small ordered domains which are separated by anti-phase boundaries (APBs). The local degree of order experience depression within these boundaries, as observed recently by Niitsu et al. [51], so APBs should contribute to the atomic disorder. Then, the ordering transition generates domains of different size and morphology, which are microstructural elements that can vary during the heat treatment procedures.

However, the comparison between such evolution of the material microstructure and the overall degree of order appears counter-intuitive for several reasons. Firstly, for instance, TEM dark-field micrographs in Ref. [32] show ordering domain growth between 3 hours and 1 week for 573 K heat treatments, Fig. 8a and b, and between 3 h and 24 h for 673 K, Fig. 8c and d. This coarsening is necessary to reduce the contribution of the boundary tension to the lattice energy and, at first glance, it could be interpreted as an increase of the overall degree of order. However, the present results contradict the last assumption indicating that stable overall degree of order is reached within the first 15 min of heat treatments. Therefore, ordering domain coarsening should be able to occur isothermally, changing the local degree of order, while holding a total overall degree of order constant. As a result of such growth, APBs density should decrease, so the system should keep a constant degree of order by either increasing the internal disorder of the  $L2_1$  domains or the thickness of the APBs. Secondly, Fig. 8a, c, and d show that the ordered domain size increases and the APB density decreases when SecHT temperature is increased from 573 K to 773 K. This fact suggests that  $L2_1$  order increases with SecHT temperature. However, present calculations and experimental results point out that thermal equilibrium order decreases with SecHT temperature, Figs. 5 and 7, and that ordering during cooling below 800 K is not enough to turn around this tendency, Fig. 6.

This apparent contradiction is originated by the assumptions that bright regions in the TEM micrographs correspond to fully ordered domains and that the brightness between images can be compared for estimating the degree of order. However, the observed domains are an integration over a certain thickness that can include different types of domains, borders and crystalline defects. The observed brightness depends on the sample thickness and microscope measuring parameters. Finally, APB apparent thickness also depends on sample thickness and the angle form between the boundary and the zone axis. Note that typically the sample thickness is not uniform in the section suitable for TEM

observations when the samples have been produced by electro-polishing. As a consequence, to perform estimations of the degree of order by comparing the brightness and domain area of different samples and, even, different positions of the same sample could be easily misleading since the analysis is extremely challenging.

Finally, while there is a good correlation between the overall degree of order and martensitic transformation temperature as shown in Fig. 6 and in previous works [21], this correlation has been found to be limited to certain circumstances. Recent experiments [32] showed that  $M_s$  dependence on SecHT duration could span for hours or even a few days. It was believed that time evolution of the degree of order could partially account for this change in  $M_s$ . However, both experimental and computational results presented here show that ODO process happens fast and overall degree of order stays stable after equilibrium has been reached within the first 15/30 min of annealing. This fact contradicts our previous assumption and points out that the SecHT time dependence of  $M_s$  should be caused by a mechanism other than a change in the overall degree of order, losing the good correlation between  $M_s$  and  $S_{L2_1}$ . Such mechanism and SecHT time dependence can be the subject of forthcoming work.

## 6. Conclusion

In this work, the kinetics of  $L2_1 \rightleftharpoons B2$  transformations in Ni–Co–Mn–In Meta-magnetic Shape Memory Alloys was analyzed theoretically by taking into account the interchanges of atoms with neighboring vacancies between the 1st nearest neighbors as well as those between the 2nd nearest neighbors. We coupled multi-scale simulation tools to investigate the kinetics of ODO in Ni–Co–Mn–In alloys which could be considered to be a relaxation phenomenon with non-equilibrium state of vacancy interchanges. Our work shows that the kinetics of ODO transition has a strong dependence on SecHT temperature. Below, 600 K, kinetics is slow, forcing the crystal to always contain a certain amount of quenched-in disorder at room temperature. Between 600 K and 750 K, kinetics is fast enough to reach thermal equilibrium state within tens of minutes during the annealing process. Above 750 K, kinetics is very fast and thermal equilibrium can be reached during heating, so no isothermal holding time is required. Experimental results based on both Curie temperature and (111) peak intensity which directly depends on  $L2_1$  order has been reported and they match well with the simulation results. The fast kinetics has ruled out the possibility that the change in the overall degree of  $L2_1$  order could contribute to the non-monotonic change of MT temperature discovered by Bruno et al. [32], other explanations should be sought to solve such phenomenon.

## Acknowledgements

First-principles calculations were carried out in the Texas A&M Supercomputing Facility at Texas A&M University as well as in the

Lonestar and Stampede Cluster at the Texas Advanced Computing Center at University of Texas, Austin. Authors would like to acknowledge the financial support of the NSF through grant DMR 1508634. TD and AT also acknowledge the partial support from NSF through grants No. 1729335 and No. 1410983. AT also acknowledges the support of the Air Force Office of Scientific Research under grant No. AFOSR-FA9550-78816-1-0180 (Program Manager: Dr. Ali Sayir).

## References

- [1] R. Kainuma, Y. Imano, W. Ito, Y. Souto, H. Morito, S. Okamoto, O. Kitakami, K. Oikawa, A. Fujita, T. Kanomata, et al., Magnetic-field-induced shape recovery by reverse phase transformation, *Nature* 439 (7079) (2006) 957–960.
- [2] P.O. Castillo-Villa, L. Mañosa, A. Planes, D.E. Soto-Parra, J. Sanchez-Llamazares, H. Flores-Zuniga, C. Frontera, Elastocaloric and magnetocaloric effects in Ni-Mn-Sn (Cu) shape-memory alloy, *J. Appl. Phys.* 113 (5) (2013), 053506.
- [3] K. Ullakko, J. Huang, C. Kantner, R. Ohandley, V. Kokorin, Large magnetic-field-induced strains in  $\text{Ni}_2\text{MnGa}$  single crystals, *Appl. Phys. Lett.* 69 (13) (1996) 1966–1968.
- [4] R. Umetsu, W. Ito, K. Ito, K. Koyama, A. Fujita, K. Oikawa, T. Kanomata, R. Kainuma, K. Ishida, Anomaly in entropy change between parent and martensitic phases in the  $\text{Ni}_{50}\text{Mn}_{34}\text{In}_{16}$  heusler alloy, *Scr. Mater.* 60 (1) (2009) 25–28.
- [5] J. Monroe, I. Karaman, B. Basaran, W. Ito, R. Umetsu, R. Kainuma, K. Koyama, Y. Chumlyakov, Direct measurement of large reversible magnetic-field-induced strain in Ni–Co–Mn–In metamagnetic shape memory alloys, *Acta Mater.* 60 (20) (2012) 6883–6891.
- [6] E. Brück, Developments in magnetocaloric refrigeration, *J. Phys. D Appl. Phys.* 38 (23) (2005) R381.
- [7] J. Barandiarán, V. Chernenko, P. Lázpita, J. Gutiérrez, J. Feuchtwanger, Effect of martensitic transformation and magnetic field on transport properties of Ni–Mn–Ga and Ni–Fe–Ga heusler alloys, *Phys. Rev. B* 80 (10) (2009), 104404.
- [8] J.-H. Chen, N.M. Bruno, I. Karaman, Y. Huang, J. Li, J.H. Ross, Direct measure of giant magnetocaloric entropy contributions in Ni–Mn–In, *Acta Mater.* 105 (2016) 176–181.
- [9] Y. Song, K.P. Bhatti, V. Srivastava, C. Leighton, R.D. James, Thermodynamics of energy conversion via first order phase transformation in low hysteresis magnetic materials, *Energy Environ. Sci.* 6 (4) (2013) 1315–1327.
- [10] B. Wang, L. Wang, Y. Liu, B. Zhao, Y. Zhao, Y. Yang, H. Zhang, Strong thermal-history-dependent magnetoresistance behavior in  $\text{Ni}_{49.5}\text{Mn}_{34.5}\text{In}_{16}$ , *J. Appl. Phys.* 106 (6) (2009), 063909.
- [11] L. Porcar, D. Bourgault, P. Courtois, Large piezoresistance and magnetoresistance effects on  $\text{Ni}_{45}\text{Co}_5\text{Mn}_{37.5}\text{In}_{12.5}$  single crystal, *Appl. Phys. Lett.* 100 (15) (2012), 152405.
- [12] N. Bruno, S. Wang, I. Karaman, Y. Chumlyakov, Reversible martensitic transformation under low magnetic fields in magnetic shape memory alloys, *Sci. Rep.* 7 (2017) 40434.
- [13] T. Kanomata, K. Shirakawa, T. Kaneko, Effect of hydrostatic pressure on the Curie temperature of the heusler alloys  $\text{Ni}_2\text{MnZ}$  (Z = Al, Ga, In, Sn and Sb), *J. Magn. Magn. Mater.* 65 (1) (1987) 76–82.
- [14] P. Entel, V. Buchelnikov, V. Khovailo, A. Zayak, W. Adeagbo, M. Gruner, H. Herper, E. Wassermann, Modelling the phase diagram of magnetic shape memory heusler alloys, *J. Phys. D Appl. Phys.* 39 (5) (2006) 865.
- [15] W. Ito, Y. Imano, R. Kainuma, Y. Souto, K. Oikawa, K. Ishida, Martensitic and magnetic transformation behaviors in heusler-type NiMnIn and NiCoMnIn metamagnetic shape memory alloys, *Metall. Mater. Trans. A* 38 (4) (2007) 759–766.
- [16] F. Guillou, P. Courtois, L. Porcar, P. Plaindoux, D. Bourgault, V. Hardy, Calorimetric investigation of the magnetocaloric effect in  $\text{Ni}_{45}\text{Co}_5\text{Mn}_{37.5}\text{In}_{12.5}$ , *J. Phys. D Appl. Phys.* 45 (25) (2012), 255001.
- [17] J. Liu, T. Gottschall, K.P. Skokov, J.D. Moore, O. Gutfleisch, Giant magnetocaloric effect driven by structural transitions, *Nat. Mater.* 11 (7) (2012) 620–626.
- [18] J. Pons, V. Chernenko, R. Santamarta, E. Cesari, Crystal structure of martensitic phases in Ni–Mn–Ga shape memory alloys, *Acta Mater.* 48 (12) (2000) 3027–3038.
- [19] V. Buchelnikov, P. Entel, S. Taskaev, V. Sokolovskiy, A. Hucht, M. Ogura, H. Akai, M. Gruner, S. Nayak, Monte Carlo study of the influence of antiferromagnetic exchange interactions on the phase transitions of ferromagnetic Ni–Mn–X alloys (X = In, Sn, Sb), *Phys. Rev. B* 78 (18) (2008), 184427.
- [20] D. Cong, S. Roth, J. Liu, Q. Luo, M. Pötschke, C. Hürrieh, L. Schultz, Superparamagnetic and superspin glass behaviors in the martensitic state of  $\text{Ni}_{43.5}\text{Co}_{6.5}\text{Mn}_{39}\text{Sn}_{11}$  magnetic shape memory alloy, *Appl. Phys. Lett.* 96 (11) (2010), 112504.
- [21] J. Monroe, J. Raymond, X. Xu, M. Nagasako, R. Kainuma, Y. Chumlyakov, R. Arroyave, I. Karaman, Multiple ferroic glasses via ordering, *Acta Mater.* 101 (2015) 107–115.
- [22] T. Graf, C. Felser, S.S. Parkin, Simple rules for the understanding of heusler compounds, *Prog. Solid State Chem.* 39 (1) (2011) 1–50.
- [23] R.W. Overholser, M. Wuttig, D. Neumann, Chemical ordering in ni-mn-ga heusler alloys, *Scr. Mater.* 40 (10) (1999) 1095–1102.
- [24] V. Recarte, J. Pérez-Landazábal, V. Sánchez-Alarcos, J. Rodríguez-Velamazán, Dependence of the martensitic transformation and magnetic transition on the atomic order in Ni–Mn–In metamagnetic shape memory alloys, *Acta Mater.* 60 (5) (2012) 1937–1945.
- [25] W. Ito, M. Nagasako, R. Umetsu, R. Kainuma, T. Kanomata, K. Ishida, Atomic ordering and magnetic properties in the  $\text{Ni}_{45}\text{Co}_5\text{Mn}_{36.7}\text{In}_{13.3}$  metamagnetic shape memory alloy, *Appl. Phys. Lett.* 93 (23) (2008), 232503.
- [26] A. Planes, L. Mañosa, E. Vives, J. Rodríguez-Carvajal, M. Morin, G. Guenin, J. Macqueron, Neutron diffraction study of long-range atomic order in Cu–Zn–Al shape memory alloys, *J. Phys. Condens. Matter* 4 (2) (1992) 553.
- [27] V. Sánchez-Alarcos, V. Recarte, J. Pérez-Landazábal, G. Cuello, Correlation between atomic order and the characteristics of the structural and magnetic transformations in Ni–Mn–Ga shape memory alloys, *Acta Mater.* 55 (11) (2007) 3883–3889.
- [28] K. Oikawa, T. Ota, T. Ohmori, Y. Tanaka, H. Morito, A. Fujita, R. Kainuma, K. Fukamichi, K. Ishida, Magnetic and martensitic phase transitions in ferromagnetic Ni–Ga–Fe shape memory alloys, *Appl. Phys. Lett.* 81 (27) (2002) 5201–5203.
- [29] V. Sánchez-Alarcos, J. Pérez-Landazábal, V. Recarte, J. Rodríguez-Velamazán, V. Chernenko, Effect of atomic order on the martensitic and magnetic transformations in Ni–Mn–Ga ferromagnetic shape memory alloys, *J. Phys. Condens. Matter* 22 (16) (2010), 166001.
- [30] B. Weise, B. Dutta, N. Teichert, A. Hütten, T. Hickel, A. Waske, Role of disorder when upscaling magnetocaloric ni-co-mn-al heusler alloys from thin films to ribbons, *Sci. Rep.* 8 (1) (2018) 9147.
- [31] S. Kustov, M. Corró, J. Pons, E. Cesari, Entropy change and effect of magnetic field on martensitic transformation in a metamagnetic Ni–Co–Mn–In shape memory alloy, *Appl. Phys. Lett.* 94 (19) (2009), 191901.
- [32] N. Bruno, D. Salas, S. Wang, I.V. Roshchin, R. Santamarta, R. Arroyave, T. Duong, Y. Chumlyakov, I. Karaman, On the microstructural origins of martensitic transformation arrest in a NiCoMnIn magnetic shape memory alloy, *Acta Mater.* 142 (2018) 95–106.
- [33] E. Cesari, D. Salas, S. Kustov, Entropy changes in ferromagnetic shape memory alloys, in: *Materials Science Forum*, vol. 684, Trans Tech Publ, 2011, pp. 49–60.
- [34] A. Pérez-Sierra, N. Bruno, J. Pons, E. Cesari, I. Karaman, Atomic order and martensitic transformation entropy change in Ni–Co–Mn–In metamagnetic shape memory alloys, *Scr. Mater.* 110 (2016) 61–64.
- [35] A. Mansouri Tehrani, H. Shahrokshahi, N. Parvin, J. Bragoch, Influencing the martensitic phase transformation in NiTi through point defects, *J. Appl. Phys.* 118 (1) (2015), 014901.
- [36] T. Hsu, Y. Linfah, The effect of quenched-in vacancies on the martensitic transformation, *J. Mater. Sci.* 18 (11) (1983) 3213–3218.
- [37] Y. Murakami, Kinetics of order-disorder transformations in the heusler  $\text{AuAgZn}_2$  alloy, *Acta Metall.* 33 (2) (1985) 167–174.
- [38] F. Fischer, J. Svoboda, F. Appel, E. Kozeschnik, Modeling of excess vacancy annihilation at different types of sinks, *Acta Mater.* 59 (9) (2011) 3463–3472.
- [39] X. Zhang, M.H. Sluiter, Ab initio prediction of vacancy properties in concentrated alloys: the case of fcc Cu–Ni, *Phys. Rev. B* 91 (17) (2015), 174107.
- [40] C. Jiang, L.-Q. Chen, Z.-K. Liu, First-principles study of constitutional point defects in b2 NiAl using special quasirandom structures, *Acta Mater.* 53 (9) (2005) 2643–2652.
- [41] J.P. Perdew, K. Burke, M. Ernzerhof, Generalized gradient approximation made simple, *Phys. Rev. Lett.* 77 (18) (1996) 3865.
- [42] H.J. Monkhorst, J.D. Pack, Special points for Brillouin-zone integrations, *Phys. Rev. B* 13 (12) (1976) 5188.
- [43] M. Methfessel, A. Paxton, High-precision sampling for Brillouin-zone integration in metals, *Phys. Rev. B* 40 (6) (1989) 3616.
- [44] A. Jain, S.P. Ong, G. Hautier, W. Chen, W.D. Richards, S. Dacek, S. Cholia, D. Gunter, D. Skinner, G. Ceder, K. A. Persson, The Materials Project: a materials genome approach to accelerating materials innovation, *APL Mater.* 1 (1) (2013), 011002, <https://doi.org/10.1063/1.4812323>. <http://link.aip.org/link/AMPADS/v1/i1/p011002/s1&Agg=doi>.
- [45] M. Doyama, J. Koehler, The relation between the formation energy of a vacancy and the nearest neighbor interactions in pure metals and liquid metals, *Acta Metall.* 24 (9) (1976) 871–879.
- [46] D. Salas, O. Oliseeva, S. Wang, T. Duong, R. Arroyave, I. Karaman, Effects of composition and crystallographic ordering on the ferromagnetic transition in Ni–Co–Mn–In magnetic shape memory alloys, *Acta Metall.*, In review.
- [47] T. Krenke, M. Acet, E.F. Wassermann, X. Moya, L. Mañosa, A. Planes, Martensitic transitions and the nature of ferromagnetism in the austenitic and martensitic states of Ni–Mn–Sn alloys, *Phys. Rev. B* 72 (1) (2005), 014412.
- [48] V. Sánchez-Alarcos, J. Pérez-Landazábal, V. Recarte, I. Lucia, J. Vélez, J. Rodríguez-Velamazán, Effect of high-temperature quenching on the magnetostuctural transformations and the long-range atomic order of Ni–Mn–Sn and Ni–Mn–Sb metamagnetic shape memory alloys, *Acta Mater.* 61 (12) (2013) 4676–4682.
- [49] P. Neibecker, M. Leitner, G. Benka, W. Petry, Increasing the achievable state of order in Ni-based heusler alloys via quenched-in vacancies, *Appl. Phys. Lett.* 105 (26) (2014), 261904.
- [50] R. Santamarta, E. Cesari, J. Font, J. Muntasell, J. Pons, J. Dutkiewicz, Effect of atomic order on the martensitic transformation of Ni–Fe–Ga alloys, *Scr. Mater.* 54 (12) (2006) 1985–1989.
- [51] K. Niitsu, K. Minakuchi, X. Xu, M. Nagasako, I. Ohnuma, T. Tanigaki, Y. Murakami, D. Shindo, R. Kainuma, Atomic-resolution evaluation of micro-segregation and degree of atomic order at antiphase boundaries in  $\text{Ni}_{50}\text{Mn}_{20}\text{In}_{30}$  heusler alloy, *Acta Mater.* 122 (2017) 166–177.